J. Fluid Mech. (2025), *vol.* 1011, A7, doi:10.1017/jfm.2025.379

Transition between rotation- and buoyancy-dominated regimes in rotating convection: the effect of boundary conditions

Veeraraghavan Kannan[1] and **Xiaojue Zhu**[1]

[1]Max Planck Institute for Solar System Research, 37077 Göttingen, Germany
Corresponding author: Xiaojue Zhu, zhux@mps.mpg.de

(Received 11 December 2024; revised 18 March 2025; accepted 3 April 2025)

In rotating convection, analysis of heat transfer reveals a distinct shift in behaviour as the system transitions from a steep scaling regime near the onset of convection to a shallower scaling at higher Rayleigh numbers (Ra), irrespective of whether the top and bottom plates have stress-free, no-slip or no boundaries (homogeneous convection). However, while most research on this transition focuses on no-slip boundary conditions, geophysical and astrophysical flows commonly involve stress-free and homogeneous convection models as well. This study delves into the transition from the rapidly rotating regime to the non-rotating one with both stress-free and homogeneous models, leveraging direct numerical simulations (DNS) and existing literature data. Our findings unveil that for stress-free boundary conditions, the transitional Rayleigh number (Ra_T) exhibits a relationship $Ra_T \sim Ek^{-12/7}$, whereas for homogeneous rotating convection, $Ra_T \sim Ek^{-2}\, Pr$, where Ek denotes the Ekman number, and Pr denotes the Prandtl number. Both of these relationships align with the data obtained through DNS.

Key words: bénard convection, turbulent convection

1. Introduction

Rotating convection serves as a fundamental paradigm in fluid dynamics, where the interplay between buoyancy-driven flow and rotation gives rise to intricate patterns and behaviours. This phenomenon is relevant across a wide range of natural and engineering systems, including atmospheric and oceanic circulation (Atkinson & Zhang 1996; Marshall & Schott 1999), as well as the dynamics of planetary interiors (Aurnou *et al.* 2015; Wicht & Sanchez 2019). In engineering applications, it plays a critical role in rotating machinery cooling systems, industrial heat exchangers and chemical reactors, where efficient thermal management is essential (Incropera & DeWitt 1996). Among the various manifestations of rotating convection, rotating Rayleigh–Bénard (RRB) convection (Plumley & Julien 2019; Kunnen 2021; Ecke & Shishkina 2023) occupies a central position, representing a canonical example that integrates buoyancy-driven flow with rotation. In the RRB convection configuration, a horizontal layer of fluid is confined between a heated bottom plate and a cooled top plate, subjected to constant rotation aligned with gravity. The three main control parameters of RRB convection are the Rayleigh number $Ra \equiv \alpha_T g L^3 \Delta/(\nu\kappa)$, the Ekman number $Ek \equiv \nu/(2\varOmega L^2)$, and the Prandtl number $Pr \equiv \nu/\kappa$, where α_T is the thermal expansion coefficient, g is the gravitational acceleration, L is the distance between the top and bottom plates, $\varDelta$ is the temperature difference across the domain, ν is the kinematic viscosity, κ is the thermal diffusivity, and $\varOmega$ is the rotation rate. The primary system response in this set-up is the Nusselt number (Nu), which is calculated as $Nu = \sqrt{Ra\,Pr}\,\langle u_z\theta\rangle_{A,t} - \langle\partial_z\theta\rangle_{A,t}$, where u_z is the vertical velocity, θ is the temperature, and $\langle\,\boldsymbol{\cdot}\,\rangle_{A,t}$ denotes a horizontal and temporal average. Here, u_z and θ are scaled using the free-fall velocity $\sqrt{\alpha_T g L\Delta}$ and $\varDelta$. Alternatively, the Nusselt number can be written in its equivalent dimensional form as $Nu = qL/\kappa\Delta$, where q is the total heat flux. In recent years, major efforts have been made, both experimentally and numerically, to approach regimes closer to those of planetary interest, where the control parameters are often extreme (van Kan *et al.* 2024). For example, in the Earth's fluid core, $Ek \approx 10^{-15}$ and $Ra \approx 10^{29}$ (Gubbins 2001; Guervilly, Cardin & Schaeffer 2019).

A key aspect of RRB convection research is understanding how Nu scales with the control parameters. For a comprehensive overview of RRBconvection, including the key scaling laws for Nu as a function of control parameters, we refer to the recent reviews by Plumley & Julien (2019), Kunnen (2021)and Ecke & Shishkina (2023). Specifically, for no-slip boundary conditions and fixed Ek, Nu increases steeply with Ra from its value unity at the onset of convection towards a shallower scaling typical of the non-rotating case. In the steep scaling regime, rotation dominates, and the Coriolis force balances the pressure gradient, a condition known as geostrophic balance (Greenspan 1969). In this rotation-dominated regime, the heat transfer scaling follows $Nu \sim (Ra/Ra_c)^{\xi} \sim (Ra\,Ek^{4/3})^{\xi}$, where $Ra_c \sim Ek^{-4/3}$ is the critical Rayleigh number for the onset of convection with rotation (Chandrasekhar 1961; Julien *et al.* 2012*b*; Stellmach *et al.* 2014). The significant effect of Ekman pumping in no-slip boundaries can lead to a very steep scaling relation $Nu \sim Ra^{3.6}Ek^{4.8}$ (Cheng *et al.* 2015), when $Pr = 7$. Cheng *et al.* (2015) report a very steep scaling for the heat transport in rotating convection, expressed as $Nu \sim (Ra\,Ek^{4/3})^{\xi}$. Crucially, their main finding is that the scaling exponent ξ is dependent on the Ekman number; specifically, as Ek decreases, ξ increases, indicating a steeper heat transport scaling under more rapid rotation. Theoretically, in extreme parameter regimes, a diffusion-free heat transport scaling $Nu \sim Ra^{3/2}Ek^2Pr^{-1/2}$ (Gillet & Jones 2006; Julien *et al.* 2012*a*), analogous to the asymptotic ultimate regime $Nu \sim Ra^{1/2}Pr^{1/2}$ in non-rotating Rayleigh–Bénard convection (Ahlers, Grossmann & Lohse 2009; Lohse & Shishkina 2024), is expected in the geostrophic turbulent regime. Recently, this scaling has been observed with no-slip boundaries at very high $Ra \gtrsim 10^{12}$ and very strong rotation $Ek \lesssim 10^{-8}$ (Song, Shishkina & Zhu 2024*b*,*c*).

Beyond the rotation-dominated regime, as the thermal driving force increases, the flow transitions into a rotation-affected regime. This regime, which marks the boundary between rotation-dominated and buoyancy-dominated regimes, has garnered considerable attention (Kunnen 2021; Ecke & Shishkina 2023). It is suggested that this transition occurs when the thermal and Ekman boundary layer thicknesses become comparable, with the transitional Rayleigh number Ra_T between the two regimes following the relation $Ra_T \sim Ek^{-7/4}$ (King *et al.* 2009), which is derived from $\delta_\theta \sim Nu^{-1} \sim Ra^{-2/7} \sim \delta_E \sim Ek^{1/2}$, where δ_θ represents the thermal boundary layer thickness, $Ra^{-2/7}$ indicates the Nu scaling for non-rotating convection, and δ_E is the Ekman layer thickness. This scaling was later refined to $Ra_T \sim Ek^{-3/2}$ (King, Stellmach & Aurnou 2012), based on the assumption that $Nu \sim Ra^{1/3}$ instead of $Nu \sim Ra^{2/7}$. This transitional scaling has been validated across various datasets under different conditions (Cheng *et al.* 2015; Kunnen 2021; Ecke & Shishkina 2023; Song *et al.* 2024*a*).

The transition from the rotation-dominated to the buoyancy-dominated regime is a fundamental aspect of rotating convection. Previous investigations have focused primarily on cases with no-slip boundary conditions, where the transition is thought to be governed by Ekman boundary layer dynamics. However, this transition is equally significant in systems with stress-free boundary conditions (Stellmach *et al.* 2014; Kunnen *et al.* 2016; Plumley *et al.* 2017; Maffei *et al.* 2021) and in homogeneous convection without boundaries (Toselli, Musacchio & Boffetta 2019), where Ekman boundary layers are absent. Note that the study utilizing an asymptotic/quasi-geostrophic model (e.g. Maffei *et al.* 2021), which assumes rapid rotation, is not designed to capture the full transitional dynamics observed in direct numerical simulations (DNS) formulations. These simplified set-ups – stress-free boundaries and homogeneous convection – provide valuable models for studying rotating fluids in geophysical and astrophysical contexts. In this context, the theory proposed by Cheng *et al.* (2015) is appealing because it does not involve Ekman layers. The theory empirically defines Ra_T as the intersection between two heat transfer scaling laws: the steep scaling $Nu \sim (Ra/Ra_c)^\xi$, typical for rapidly rotating convection, and the shallow non-rotating scaling $Nu \sim Ra^\alpha$. By equating these trends, the transition is predicted as $Ra_T \sim Ek^{-4\xi/3(\xi-\alpha)}$. Using $\xi = 3$, the characteristic scaling exponent in rapidly rotating convection with no-slip boundaries (King *et al.* 2012; Song *et al.* 2024*c*), and $\alpha = 1/3$, the typical exponent for non-rotating Rayleigh–Bénard convection in the classical regime (Malkus 1954; Ahlers *et al.* 2009), Cheng *et al.* (2015) derived $Ra_T \sim Ek^{-3/2}$ as well. Motivated by this framework, we employ DNS to study the transition under stress-free boundary conditions, and incorporate data from homogeneous rotating convection provided by Toselli *et al.* (2019). Beyond investigating the transition through Nu, we also show that the transition can be characterized and predicted using the Reynolds number ($Re = uL/\nu$), where u is the root mean square velocity. This additional system response offers further confirmation of the same transitional behaviour.

2. Numerical details

The current DNS employ the Boussinesq approximation to model RRB convection in a fluid confined between two horizontal plates. The system is subjected to a constant angular velocity $\varOmega$ around the vertical axis z, with gravitational acceleration $\boldsymbol{g} = -g\boldsymbol{e}_z$, where $\boldsymbol{e}_z$ is the unit vector in the vertical direction. The reference scales used in this study are the height of the domain L, the temperature difference between the plates $\varDelta$, and the characteristic free-fall velocity $U_{ff} = \sqrt{\alpha_T g L \Delta}$. The dimensionless variables for temperature θ, velocity $\boldsymbol{u}$, pressure p, and time t are defined based on these scales. The resulting dimensionless governing equations for the incompressible fluid flow are

$$\nabla \cdot \boldsymbol{u} = 0, \tag{2.1}$$

$$\frac{\partial \boldsymbol{u}}{\partial t}+\boldsymbol{u}\cdot\nabla\boldsymbol{u}=-\nabla p+\sqrt{\frac{Pr}{Ra}}\,\nabla^2\boldsymbol{u}+\theta\boldsymbol{e}_z-\frac{1}{Ek}\sqrt{\frac{Pr}{Ra}}\,\boldsymbol{e}_z\times\boldsymbol{u}, \tag{2.2}$$

$$\frac{\partial \theta}{\partial t}+\boldsymbol{u}\cdot\nabla\theta=\frac{1}{\sqrt{Ra\,Pr}}\,\nabla^2\theta. \tag{2.3}$$

To solve the governing equations, the energy-conserving second-order finite-difference code AFiD was employed (Verzicco & Orlandi 1996; van der Poel *et al.* 2015; Zhu *et al.* 2018). The code was parallelized using a two-dimensional pencil domain decomposition strategy (van der Poel *et al.* 2015) and GPU acceleration (Zhu *et al.* 2018) for large-scale DNS. The simulations applied stress-free boundary conditions with a constant temperature at the top and bottom plates, along with periodic boundary conditions in both horizontal directions.

The grid points were distributed using a Chebyshev-like scheme in the wall-normal (z) direction, clustering points near the top and bottom plates, while a uniform distribution was used in the periodic (x and y) directions. This arrangement ensures that at least 10 grid points are always present within the thermal boundary layer.

Additionally, to assess the grid resolution used in the DNS, we calculated the mean dimensionless Kolmogorov microscale, defined as $\eta/L=(\tilde{\nu}^3/\langle\tilde{\epsilon}\rangle_V)^{1/4}$, where $\tilde{\nu}=\sqrt{Pr/Ra}$ is the dimensionless viscosity, and $\langle\tilde{\epsilon}\rangle_V$ is the volume- and time-averaged dimensionless kinetic energy dissipation rate. The maximum ratio of the mesh size to the mean Kolmogorov microscale remains below 2.2 in all simulations, a threshold that has been found empirically to be acceptable in rotating convection simulations (Verzicco & Camussi 2003; Shishkina *et al.* 2010; Scheel, Emran & Schumacher 2013).

All simulations were performed using $Pr=1$ and were run long enough to achieve saturation of thermal and kinetic energies, ensuring statistically steady flow states, and allowing the inverse energy cascade to saturate, particularly in cases exhibiting large-scale vortices with no evidence of secular growth. Moreover, ensemble averages were taken over 200 free-fall time units after reaching the saturation state.

To ensure accuracy, the convergence of Nu was thoroughly checked across the entire domain. The maximum relative error in Nu, calculated using five different methods (as outlined in Stevens, Verzicco & Lohse 2010), was kept below 1 %. The explored parameter range, along with the corresponding grid resolution and transport parameters in the present DNS of stress-free RRBconvection, is summarized in Appendix A.

3. Scalings and flow structures in DNS with stress-free boundaries

Inspection of the mid-plane horizontal cross-section contours of fluctuating temperature (figure 1), vertical vorticity (figure 2) and the vertical cross-section of vertical velocity (figure 3) for varying $Ra\in[1.3\times10^8, 5\times10^{10}]$ at a fixed $Ek=5\times10^{-6}$ with stress-free boundaries suggests that the flow can be classified qualitatively into several distinct regimes. While some studies adopt a detailed classification that includes cells, Taylor columns, plumes, geostrophic turbulence (where large-scale vortices form), and eventually regimes where rotation becomes negligible, our work focuses primarily on the transition between rotation-dominated and buoyancy-dominated states (Sprague *et al.* 2006; Julien *et al.* 2012*b*). The cellular regime is characterized by columns that extend across the fluid layer, formed due to the dominance of strong rotational effects over buoyancy forces. These cells are encased in ’sleeves’ of cold fluid, which act as insulating layers and limit interaction between adjacent columns. In contrast, the Taylor columns regime, characterized by vertically coherent columnar structures, is typically observed for fluids

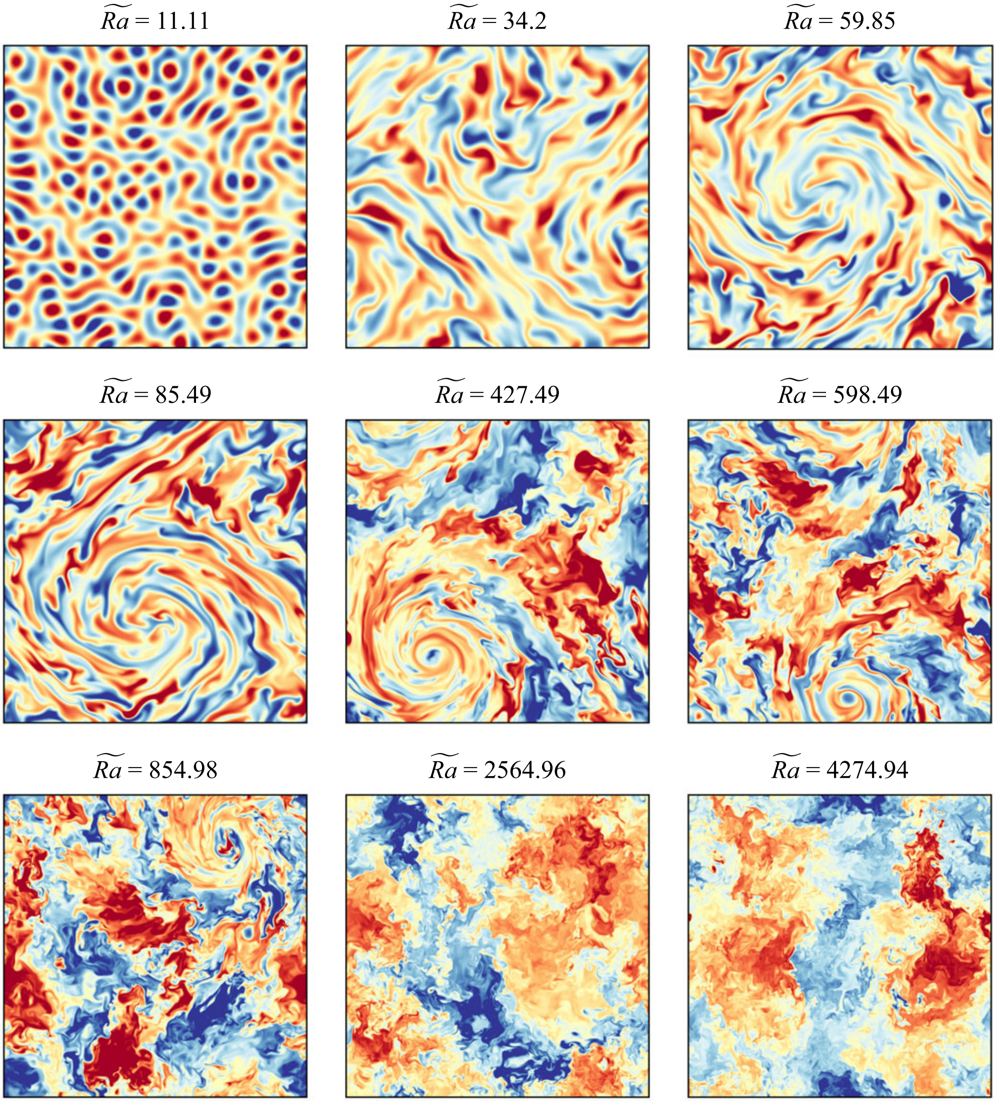

Figure 1. Horizontal cross-sections of the instantaneous contours of fluctuating temperature θ for stress-free RRB convection at the mid-plane is shown for varying Ra, with fixed $Ek = 5 \times 10^{-6}$ and $Pr = 1$. Here, red (blue) denotes positive (negative) temperature fluctuations. The nine plots correspond to a range of the supercriticality parameter, $10 < \widetilde{Ra} \equiv Ra\, Ek^{4/3} < 4275$.

with $Pr > 1$ (Julien *et al.* 2012*b*). However, as Ra increases, the insulating effect diminishes, leading to greater interaction between the columns. This reduction in column length signals the transition to the large-scale vortex regime, where vortices intensify and occupy the entire domain (Julien *et al.* 2012*b*; Favier, Silvers & Proctor 2014; Guervilly, Hughes & Jones 2014; Rubio *et al.* 2014; Favier, Guervilly & Knobloch 2019; Aguirre Guzmán *et al.* 2021; Maffei *et al.* 2021; De Wit, Van Kan & Alexakis 2022). As Ra continues to rise, the large-scale vortices transition from a cyclone–anticyclone dipole structure to a cyclonic structure within an anticyclonic sheath, which eventually disappears. The flow then transitions to a buoyancy-dominated turbulence regime, where

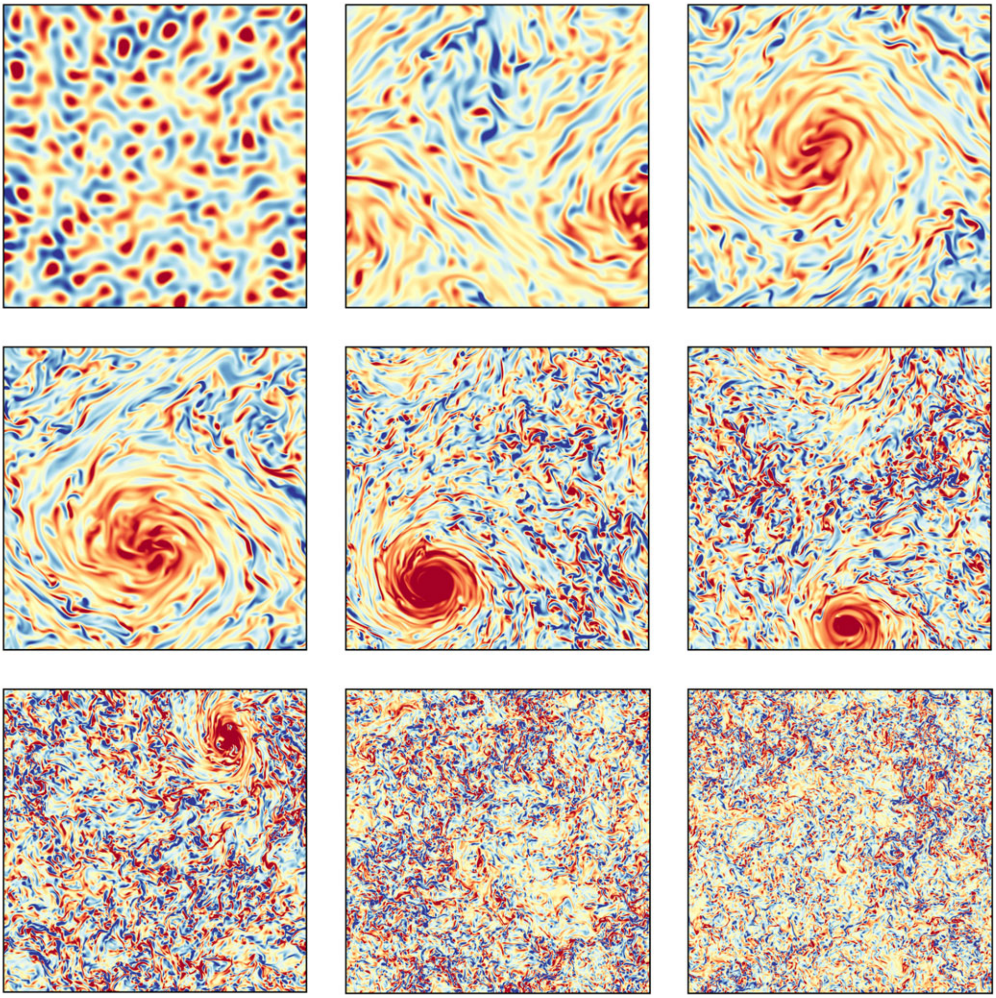

Figure 2. Horizontal cross-sections of the instantaneous contours of vertical vorticity ω_z for the same flow conditions as in figure 1. Here, red (blue) denotes positive (negative) vorticity.

the influence of rotation becomes very weak or negligible, and the flow behaviour aligns with classical non-rotating Rayleigh–Bénard convection.

An overview of the characteristics of RRB convection from the beginning of the onset can also be seen in the Nu measurements, covering a wide range of Ra and Ek values (see figure 4*a*). The rapid rise from the conduction value $Nu = 1$ represents the nonlinear growth from onset and a region of rotation-dominated dynamics at $Ra > Ra_c$, where Ra_c is the critical Rayleigh number for onset. As demonstrated by these data, the range of Ra spanned in this rotation-dominated region increases with decreasing Ek. The scaling behaviour of Nu in the rotation-dominated regime provides insights into how heat transport is influenced by the interplay of buoyancy and rotational forces. For stress-free boundary conditions, the heat transport follows the scaling $Nu \sim Ra^{3/2} Ek^2$ in a wide range in the rotation-dominated regime, as shown in figure 4(*b*). This scaling is consistent with predictions for the diffusion-free regime, where thermal and momentum transport are not constrained by diffusivity (Stevenson 1979; Gillet & Jones 2006; Julien *et al.* 2012*a*, 2016; Stellmach *et al.* 2014; Cheng & Aurnou 2016; Plumley *et al.* 2017;

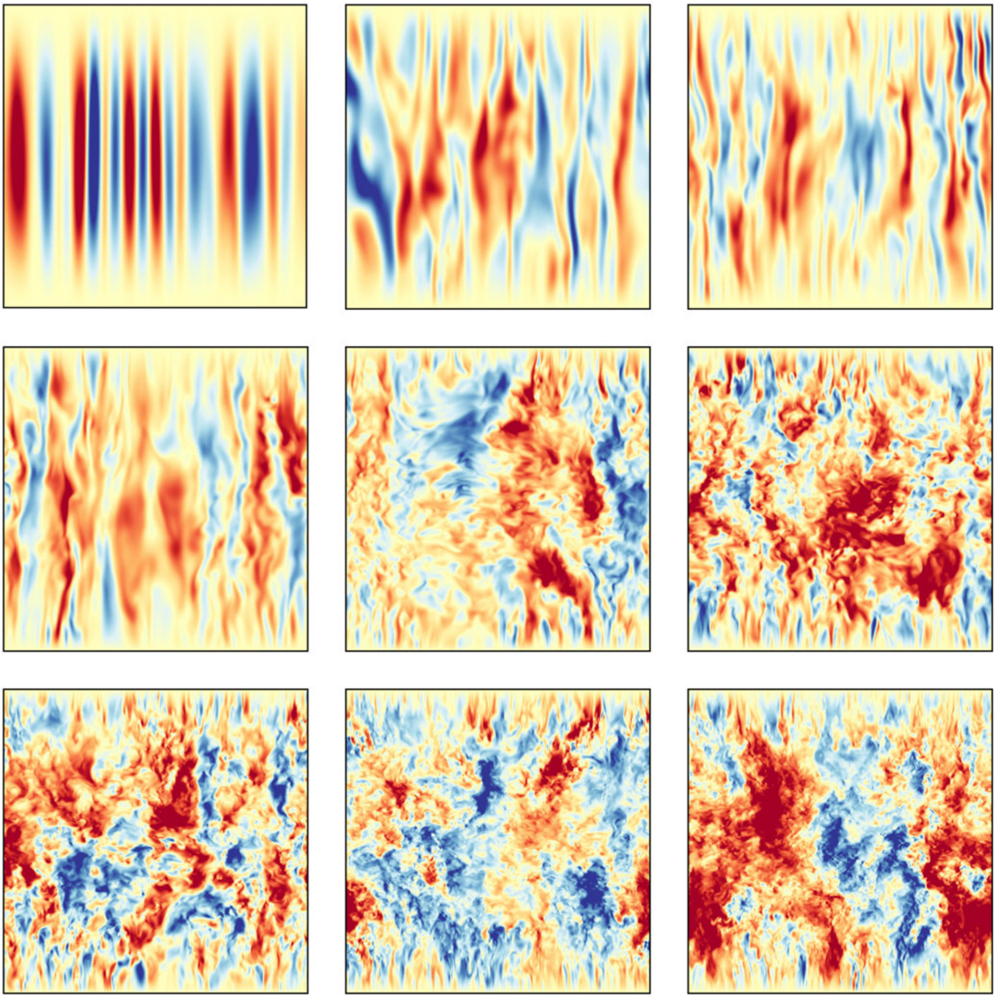

Figure 3. Vertical cross-sections of the instantaneous contours of vertical velocity u_z for the same flow conditions as in figure 1. Here, red (blue) denotes positive (negative) velocity.

Bouillauta *et al.* 2021; Maffei *et al.* 2021; Oliver *et al.* 2023; van Kan *et al.* 2024; Song *et al.* 2024*c*). Notably, the 3/2 scaling in the stress-free case can be observed at relatively high Ek ($Ek = 5 \times 10^{-7}$) (Julien *et al.* 2012*a*; Stellmach *et al.* 2014; Plumley *et al.* 2017), in contrast to the no-slip boundary condition cases, where the 3/2 scaling is limited to extremely low Ek ($Ek = 5 \times 10^{-9}$) (Song *et al.* 2024*c*). As Ra increases further at constant Ek, the balance of rotation and buoyancy shifts, such that Nu approaches the non-rotating convection curve $Nu \sim Ra^{1/3}$, the so-called classical regime (Ahlers *et al.* 2009; Lohse & Shishkina 2024). Note that the scaling observed in non-rotating Rayleigh–Bénard convection with stress-free boundary conditions is comparable to that with no-slip boundary conditions (Petschel *et al.* 2013).

Within the studied parameter regime – where the dynamics is governed by a balance between the Coriolis force and buoyancy – the Nusselt number exhibits a scaling transition from $Ra^{3/2}$ to $Ra^{1/3}$. This behaviour aligns with theoretical predictions and previous experimental and numerical studies (Ahlers *et al.* 2009; Julien *et al.* 2012*b*; Cheng *et al.* 2015). Although the $Ra^{3/2}$ scaling is often interpreted as indicative of a diffusion-free

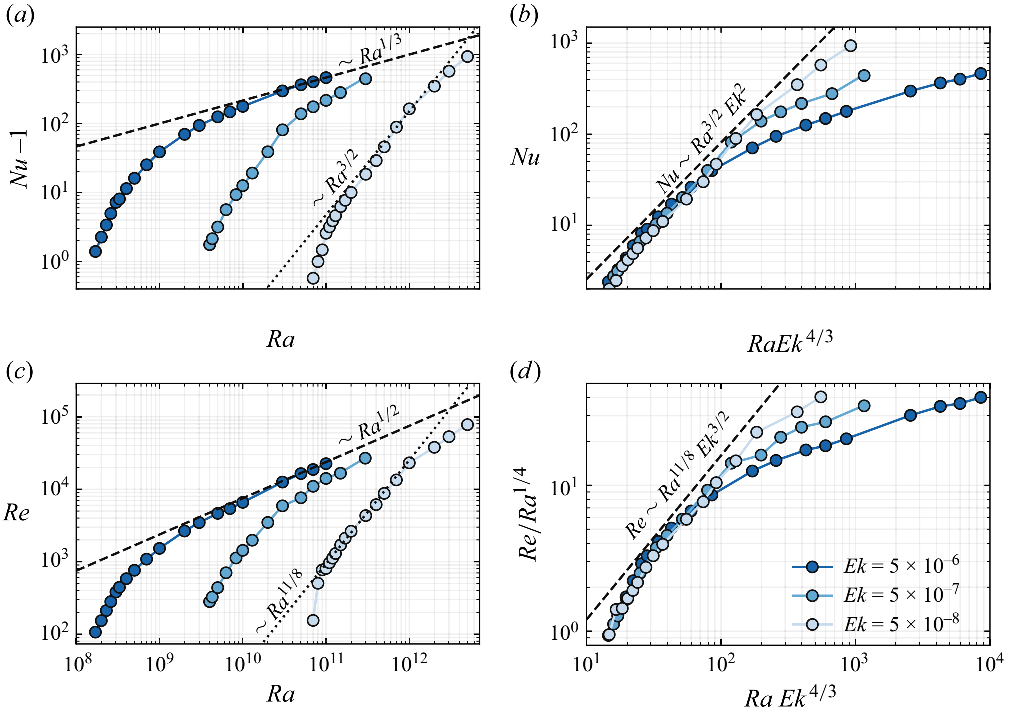

Figure 4. (*a*) Dimensionless heat transport ($Nu - 1$) and (*c*) momentum transport (Re) versus Ra for various Ek, obtained from DNS of RRB convection with stress-free boundaries and $Pr = 1$. Black dashed lines show non-rotating convection scalings ($Nu - 1 \sim Ra^{1/3}$, $Re \sim Ra^{1/2}$), and dotted lines indicate geostrophic turbulence scalings ($Nu - 1 \sim Ra^{3/2}$, $Re \sim Ra^{11/8}$). Plots of (*b*) Nu and (*d*) Re, normalized by $Ra^{1/4}$, as functions of the supercriticality parameter $Ra\, Ek^{4/3}$. Dashed lines represent rotation-dominant regime scalings ($Nu \sim Ra^{3/2} Ek^2$, $Re \sim Ra^{11/8} Ek^{3/2}$). Here, for stress-free cases, Re is defined based on u_z, as the horizontal velocity is significantly larger than the vertical velocity due to the strong inverse energy cascade. Therefore, the horizontal velocity does not characterize the heat transfer effectively.

regime, our analysis reveals that other dynamics remain influenced by diffusive processes. This is evidenced by a Reynolds number scaling (see discussion below) that deviates from the diffusion-free expectation. Hence the observed transition does not signify a complete shift from a truly diffusion-free state to a diffusive state. Rather, for stress boundary conditions, both of the regimes remain diffusive for the data range that we explored.

To assess whether the diffusion-free regime has been achieved conclusively for stress-free cases, we analyse the scaling of Re as a function of Ra across various Ek. Figure 4(*c*) depicts Re versus Ra, showing a steep increase in Re at lower Ra within the rotation-dominated regime. In the range of Ra where diffusion-free heat transfer is observed, Re follows the scaling $Re \sim Ra^{11/8} Ek^{3/2}$ (see figure 4*d*), which deviates significantly from the diffusion-free Reynolds scaling $Re \sim Ra\, Ek$ (Aurnou, Horn & Julien 2020; Song *et al.* 2024*c*). Consequently, even though the heat transfer scaling exponent reaches 3/2, the Reynolds number does not adhere to the expected linear Ra dependence. This indicates that the true diffusion-free regime has not yet been realized in the stress-free DNS. In the next section, we will demonstrate that this observed scaling can be derived from the transitional scaling Ra_T. As Ra increases further,the Re scaling (again similar to the no-slip counterpart), just like Nu, gradually approaches the non-rotating convection relation $Re \sim Ra^{1/2}$ (Ahlers *et al.* 2009; Lohse & Shishkina 2024), marking the transition

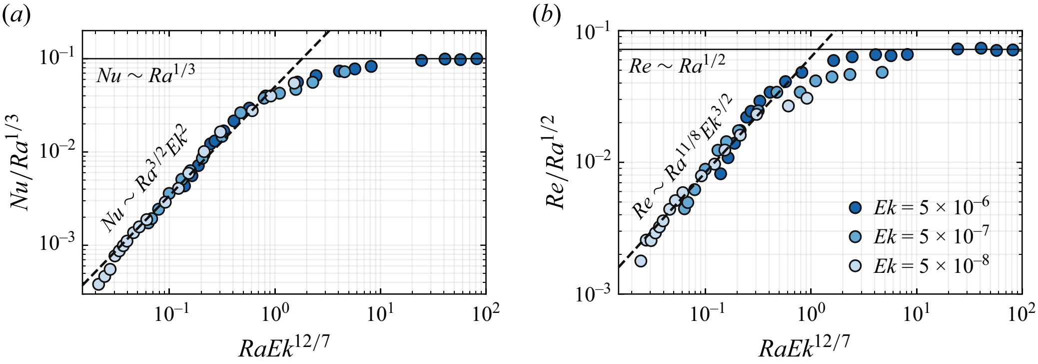

Figure 5. Transition in stress-free RRB convection: (*a*) Nusselt number (Nu) normalized by $Ra^{1/3}$, and (*b*) Reynolds number (Re) normalized by $Ra^{1/2}$, are shown as functions of Ra, normalized by the transitional Rayleigh number $Ra_T \sim Ek^{-12/7}$ for different Ek at fixed $Pr = 1$.

to buoyancy-dominated dynamics. This shift reflects a regime where buoyancy forces dominate rotational influences, fundamentally altering the flow behaviour.

4. Transition with stress-free boundary condition

As discussed in § 1, the transition between the rotation- and buoyancy-dominated regimes in RRB convection can be determined by equating the Nu scaling laws for the two regimes. For the no-slip boundary condition, $Ra_T \sim Ek^{-3/2}$ is obtained by equating $Nu \sim Ra^3 Ek^4$, a typical scaling for the rotation-dominated regime, with $Nu \sim Ra^{1/3}$, the classical scaling for the buoyancy-dominated regime. It is important to note that if Ra_T exists, then the scaling relations for both Nu and Re should yield consistent results. From Song *et al.* (2024*c*), it is known that when $Nu \sim Ra^3 Ek^4$, the Reynolds number follows $Re \sim Ra^{5/2} Ek^3$. In the classical regime of non-rotating Rayleigh–Bénard convection, Re scales close to $Re \sim Ra^{1/2}$. Equating these two Re scalings also leads to $Ra_T \sim Ek^{-3/2}$, reinforcing the consistency of the scaling arguments derived from both heat and momentum transport.

Now we come to the stress-free boundary condition cases. In the rotation-dominated regime for stress-free RRBconvection, the typical scaling is $Nu \sim Ra^{3/2} Ek^2$, while in the buoyancy-dominated regime, the scaling is again the classical $Nu \sim Ra^{1/3}$. By equating these two scalings, the transitional Ra is derived as $Ra_T \sim Ek^{-12/7}$ for stress-free boundary conditions. This prediction for Ra_T is verified using DNS data for the stress-free case, as shown in figures 5(*a*) and 5(*b*) for both Nu and Re. While the transition $Ra_T \approx \mathcal{O}(10)\ Ek^{-12/7}$ is clearly observed at $Ek = 5 \times 10^{-6}$, for $Ek = 5 \times 10^{-7}$ and $Ek = 5 \times 10^{-8}$, the available data suggest a similar trend, although the range of Ra explored is more restricted due to computational constraints, and will be verified in the future.

It is observed that beyond Ra_T, both Nu and Re approach their non-rotating values, indicating that the flow has transitioned into the buoyancy-dominated regime. Additionally, using the scaling $Ra_T \sim Ek^{-12/7}$, the Re value in the rotation-dominated regime for stress-free RRB convection can also be derived as $Re \sim Ra^{11/8} Ek^{3/2}$ (see figure 4*c*,*d*) by equating the scaling for the buoyancy-dominated region, where $Re \sim Ra^{1/2}$, with the scaling of Ra_T.

In stress-free rotating convection, the classical diffusion-free scaling $Re \sim Ra\, Ek$ is expected when inertial effects are negligible. However, our analysis reveals that the

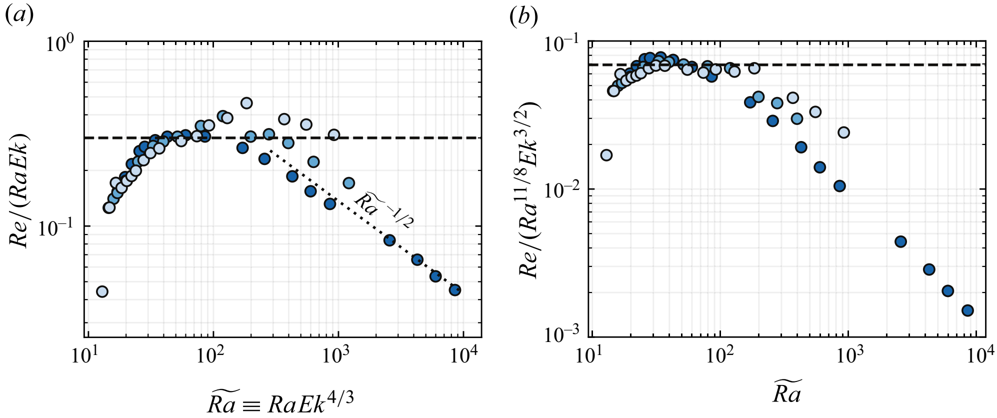

Figure 6. Dimensionless momentum transport Re, normalized by (*a*) diffusion-free $Ra\,Ek$ scaling and (*b*) $Ra^{11/8}Ek^{3/2}$ scaling proposed in this work, shown as a function of supercriticality $\widetilde{Ra} = Ra\,Ek^{4/3}$.

formation of large-scale vortices leads to enhanced momentum transport, resulting in a scaling $Re \sim Ra^{11/8}\,Ek^{3/2}$. Figure 6 again illustrates that at moderate Ra, the measured Reynolds number follows the steeper $Ra^{11/8}\,Ek^{3/2}$ trend, consistent with the impact of the inverse energy cascade associated with large-scale vortices formation.

Recent numerical simulations by Oliver *et al.* (2023), employing an asymptotically reduced model, suggest a scaling $Re \sim \widetilde{Ra}^{1.325}$ based on an empirical fit to their data within the range $40 \leqslant \widetilde{Ra} \leqslant 200$. This exponent is close to the $11/8 = 1.375$ scaling obtained in the present work for moderately supercritical parameters.

Additionally, for a fixed rotation rate (fixed Ek) but increasing Ra, the transport properties tend towards those in the non-rotating case, i.e. $Re \sim Ra^{1/2}$, denoting the transition from a rotation-dominatedregime to a buoyancy-dominated regime. This behaviour is fully captured by the scaling $Re/(Ra\,Ek) \sim \widetilde{Ra}^{-1/2}$, shown as a dotted line in figure 6(*a*).

Having examined the transition based on the scaling laws of Nu at different regimes in the RRB convection framework, it is also worthwhile to consider the transition based on the convective Rossby number Ro, which is defined as the ratio of thermal buoyancy to the Coriolis force. It has been argued that the convection regime dominated by rotation extends from the onset of rotating convection up to where $Ro \lesssim 1$ (Zhong & Ahlers 2010; Stevens, Clercx & Lohse 2013). However, it has been shown that the Ro normalization does not accurately define the transition. Our results, as shown in figure 7(*a*) for the stress-free RRB convection cases, are consistent with previous observations (King *et al.* 2009; Cheng *et al.* 2015). These observations suggest that distinctly smaller scale motions contribute to convective heat transfer, and the system scale parameter Ro does not collapse the data well.

Alternatively, local Rossby numbers are defined in the literature to predict the transition. This is given by the expression (Christensen & Aubert 2006; Sreenivasan & Jones 2006)

$$Ro_\ell = \frac{U}{2\Omega\ell} = \sqrt{\frac{Ra}{Pr}}\,Ek\,\frac{L}{\ell}. \tag{4.1}$$

This formulation was used by Cheng *et al.* (2015) to test whether Ro_ℓ can predict the rotation-dominant and buoyancy-dominant transitions in RRB convection simulations. However, in their experiments, they were unable to measure velocities directly, so they

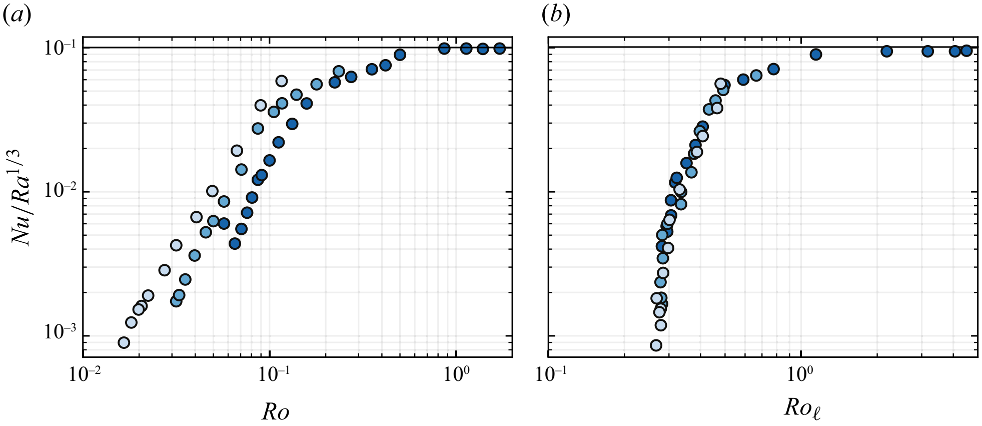

Figure 7. Transition in stress-free RRB convection based on Rossby number, with Nu normalized by $Ra^{1/3}$ shown as a function of (*a*) convective Rossby number Ro and (*b*) local Rossby number $Ro_\ell = Ro \times L/\ell$ based on convective length scale ℓ/L.

rewrote the equation as $Ro_\ell = \sqrt{(Ra/Pr)}\ Ek\ (L/\ell)$, substituting $\ell \sim Ek^{1/3}$ and assuming $Re \sim (Nu-1)^{1/2} Ra^{1/2} Ek^{1/3}/Pr$. This formulation allowed them to collapse the data well for $Pr \approx 7$.

In contrast, our work is based on DNS, so we directly computed the time-averaged dominant length scale from the vertical velocity spectra, and substituted it into the Ro_ℓ formulation. As shown in figure 7(*b*), we find that this formulation predicts the transition more accurately compared to Ro, even for the $Pr = 1$ simulations performed in this study. For $Ro_\ell > 1$, the flow approaches the buoyancy-dominated regime. It is important to note that the depth-averaged flow is subtracted from the total flow when computing the length scale, particularly for cases exhibiting large-scale vortices.

5. Transition in the homogeneous rotating condition

Homogeneous rotating convection refers to a simplified configuration of RRB convection in which the effects of solid boundaries are removed. The flow occurs in an unbounded, periodic domain and is driven by an imposed linear temperature gradient in the vertical direction, which is parallel to both the rotational and gravitational axes. This paradigm is also frequently employed to investigate the ultimate turbulent state predicted by Kraichnan (1962). Such a state is theorized to arise in Rayleigh–Bénard convection when the boundary layer contribution to heat transfer becomes negligible (Grossmann & Lohse 2004). Numerical experiments have demonstrated that this set-up exhibits the ultimate regime both with and without rotation (Lohse & Toschi 2003; Calzavarini *et al.* 2005; Toselli *et al.* 2019). By eliminating Ekman boundary layers, this configuration serves as a valuable model for studying geophysical and astrophysical flows, where boundary effects are minimal.

Additionally, while both homogeneous convection and stress-free convection eliminate Ekman boundary layers, they differ in domain geometry. In homogeneous convection, the absence of physical boundaries – with periodic boundary conditions applied in all directions – removes not only Ekman layers but also any wall-induced constraints, resulting in distinct flow dynamics. In contrast, stress-free convection remains confined between two plates, which impose discrete vertical modes and influence the thermal boundary layers. These geometric differences can lead to distinct transitional scaling

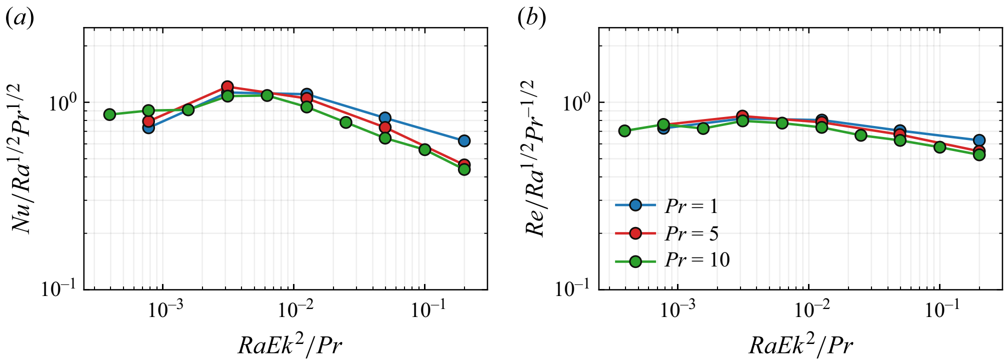

Figure 8. Transition in homogeneous RRB convection: (*a*) Nu normalized by $Ra^{1/2}Pr^{1/2}$, and (*b*) Re normalized by $Ra^{1/2}Pr^{-1/2}$, shown as functions of Ra, normalized by $Ra_T \sim Ek^{-2}Pr$ for different Pr. Data are taken from DNS by Toselli *et al.* (2019).

behaviours, with stress-free convection exhibiting different scaling properties compared to homogeneous convection.

Notably, in homogeneous rotating convection, both the rotation-dominated and buoyancy-dominated regimes correspond to the diffusion-free ultimate regime. This dual correspondence underscores the asymptotic nature of transport dynamics in such flows.

In the rotation-dominated regime, Nu scales as $Nu \sim Ra^{3/2}Ek^2Pr^{-1/2}$ (Aurnou *et al.* 2020; Song *et al.* 2024*c*), reflecting the diffusion-free regime scaling. In contrast, the buoyancy-dominated regime follows the scaling $Nu \sim Ra^{1/2}Pr^{1/2}$ (Lohse & Toschi 2003; Toselli *et al.* 2019), where buoyancy forces dominate, and the transport characteristics align with the ultimate regime for non-rotating convection. By equating these two diffusion-free scaling laws for Nu, Ra_T is derived as $Ra_T \sim Ek^{-2}Pr$. Similarly, Re exhibits scaling behaviour consistent with the diffusion-free regime. In the rotation-dominated regime, $Re \sim Ra\, Ek\, Pr^{-1}$ (Aurnou *et al.* 2020; Song *et al.* 2024*c*). In the buoyancy-dominated regime, $Re \sim Ra^{1/2}Pr^{-1/2}$ (Toselli *et al.* 2019; Lohse & Shishkina 2024), again reflecting the asymptotic scaling of turbulent convection without rotational constraints. Equating these two scalings for Re leads to the same relation, i.e. $Ra_T \sim Ek^{-2}Pr$. The consistency of Ra_T obtained from both Nu and Re confirms the robustness of this approach and underscores the diffusion-free nature of transport in both regimes.

The scaling for Ra_T is validated using DNS data from Toselli *et al.* (2019) for homogeneous convection at $Ra = 1.1 \times 10^7$ and 2.2×10^7, $Pr \in \{1, 5, 10\}$ and $Ek \in [3 \times 10^{-4}, 6 \times 10^{-6}]$. Figure 8(*a*,*b*) present Nu and Re from the DNS data plotted against the predicted Ra_T scaling. For the available dataset, the Ra_T scaling demonstrates good data collapse, suggesting that the overall dynamics is well captured by the predicted scaling. This indicates that Ra_T for the homogeneous case can be estimated reliably using the proposed theory.

It is worth noting that the primary focus of Toselli *et al.* (2019) was to examine heat transfer enhancement in the weakly rotating regime. Consequently, the steep scaling regime – expected to appear on the left-hand side of the figure ($Ra\, Ek^2/Pr < 10^{-4}$)–is not represented in the data. Although the current dataset does not include additional points in the transition region due to inherent limitations in the simulation parameter range, the observed trend remains consistent with the expected transition behaviour. We acknowledge that the present data may not fully capture the detailed dynamics of the transition, and future investigations with an extended parameter space are planned to further elucidate these dynamics.

Boundary condition	Rotation-dominant regime	Buoyancy-dominant regime	Transitional scaling
No-slip	$Nu \sim Ra^3 Ek^4$	$Nu \sim Ra^{1/3}$	$Ra_T \sim Ek^{-3/2}$
	$Re \sim Ra^{5/2} Ek^3$	$Re \sim Ra^{1/2}$	$Ra_T \sim Ek^{-3/2}$
Stress-free	$Nu \sim Ra^{3/2} Ek^2$	$Nu \sim Ra^{1/3}$	$Ra_T \sim Ek^{-12/7}$
	$Re \sim Ra^{11/8} Ek^{3/2}$	$Re \sim Ra^{1/2}$	$Ra_T \sim Ek^{-12/7}$
Homogeneous	$Nu \sim Ra^{3/2} Ek^2 Pr^{-1/2}$	$Nu \sim Ra^{1/2} Pr^{1/2}$	$Ra_T \sim Ek^{-2} Pr$
convection	$Re \sim Ra Ek Pr^{-1}$	$Re \sim Ra^{1/2} Pr^{-1/2}$	$Ra_T \sim Ek^{-2} Pr$

Table 1. Scaling for Nu and Re in the rotation- and buoyancy-dominated regimes for different boundary conditions in RRB convection, as well as for homogeneous convection, along with the scaling of Ra_T, calculated from both Nu and Re. Note that for the no-slip and stress-free boundary conditions, the scaling relations do not include Prandtl number dependence, as simulations were conducted at a fixed $Pr = 1$. For the homogeneous case, Pr dependence is included explicitly, reflecting theoretical scalings and the dataset's Pr variation.

This approach – equating the transport parameter scalings (both Nu and Re) in the rotation-dominated and buoyancy-dominated regimes–proves robust for predicting the transitional Rayleigh number across different boundary condition set-ups within the RRB convection framework. The different scalings for no-slip, stress-free and homogeneous RRB convection are summarized in table 1. These scalings reflect the transition between rotation-dominated and buoyancy-dominated regimes. It is important to note that for the no-slip and stress-free boundary conditions, the scaling relations presented in table 1 do not include a dependence on the Prandtl number, as the simulations were conducted and the scalings were verified at a fixed $Pr = 1$. In contrast, for the homogeneous case, the scaling relations explicitly incorporate the Prandtl number, reflecting both theoretical considerations and the variation in Pr across the dataset used in Toselli *et al.* (2019).

It is also important to emphasize that the homogeneous convection model adopted in this study is an idealized framework designed to isolate the intrinsic, diffusion-free turbulent transport mechanisms in rotating convection. Although geophysical and astrophysical convective layers are indeed bounded – such as Earth's liquid outer core, which is confined between the solid inner core and the overlying mantle – the effective boundary conditions in these systems can, in some cases, approximate stress-free or even partially free-slip conditions rather than the strict no-slip condition often assumed in laboratory experiments. In this regard, homogeneous convection serves as a useful reference model that strips away the complexities introduced by boundary layers, allowing us to test and validate the diffusion-free scaling laws in the interior flow. We stress that this approach is intended to complement, not replace, more realistic bounded models. In practice, the insights gained from homogeneous convection help to clarify how boundary effects modify the transition between rotation- and buoyancy-dominated regimes in fully bounded systems.

6. Concluding remarks

This study investigated the transition between rotation- and buoyancy-dominated regimes in RRB convection under stress-free and homogeneous boundary conditions. Using DNS and theoretical analysis, we established the scaling for the transitional Rayleigh number Ra_T, which characterizes the transition from the rotation-dominated regime tothe buoyancy-dominated regime, as a function of control parameters in RRB convection. The scaling for Ra_T was derived by equating the scaling laws for Nusselt and Reynolds numbers, in both the rotation-dominated and buoyancy-dominated regimes.

The scaling was consistent regardless of whether heat or momentum transport was analysed, with $Ra_T \sim Ek^{-12/7}$ for stress-free boundary conditions, and $Ra_T \sim Ek^{-2} Pr$ for homogeneous conditions. These findings extend the established scaling frameworks developed for no-slip boundary conditions and offer new insights into the effects of boundary conditions on convective transitions.

In the asymptotic limit, the reduced Rayleigh number $Ra\, Ek^{4/3}$ is assumed to be of order 1, which implies $Ra_T\, Ek^{4/3} \sim Ek^{-1/3}$ (Julien *et al.* 2012*b*; Maffei *et al.* 2021), hence $Ra_T \sim Ek^{-5/3}$. Our DNS results for stress-free boundary conditions indicate that the transitional Rayleigh number scales as $Ra_T \sim Ek^{-12/7}$, with exponent approximately -1.71. This is in close agreement with the asymptotic prediction $-5/3 \approx -1.67$, and the small difference can likely be attributed to finite-amplitude effects and higher-order corrections. For homogeneous (triply periodic) convection, the scaling $Ra_T \sim Ek^{-2}$ reflects the distinct flow dynamics that arises in the absence of physical boundaries.

The present work lays the groundwork for exploring extreme regimes relevant to planetary and stellar environments, where stress-free or homogeneous (boundary-free) conditions are more representative. Future research could build upon this foundation by investigating a wider range of Prandtl numbers and rotation rates, further broadening the applicability of these insights to the complex dynamics of rotating fluids.

Acknowledgements. We gratefully acknowledge the financial support from the Max Planck Society and the German Research Foundation through grants 521319293, 540422505 and 550262949. All the simulations have been conducted on the HPC systems of the Max Planck Computing and Data Facility (MPCDF) as well as the National High Performance Computing (NHR@ZIB and NHR-Nord@Göttingen).

Declaration of interests. The authors report no conflict of interest.

Appendix A. Numerical parameters and grid resolutions

The range of parameters investigated, together with the associated grid resolution and transport parameters, for the current DNS of stress-free RRB convection is outlined in Table 2.

Case no.	Ek	Ra	$\widetilde{Ra}$	Ro	$\varGamma$	$N_x \times N_y \times N_z$	Nu	Re
1	5×10^{-6}	1.3×10^{8}	11.11	0.06	2	$960 \times 960 \times 240$	1.83	63.57
2	5×10^{-6}	1.7×10^{8}	14.53	0.07	2	$960 \times 960 \times 240$	2.40	106.70
3	5×10^{-6}	2×10^{8}	17.10	0.07	2	$1024 \times 1024 \times 256$	3.26	153.40
4	5×10^{-6}	2.3×10^{8}	19.66	0.08	2	$1024 \times 1024 \times 256$	4.38	211.51
5	5×10^{-6}	2.6×10^{8}	22.23	0.08	2	$1024 \times 1024 \times 256$	5.96	281.29
6	5×10^{-6}	3×10^{8}	25.65	0.09	2	$1024 \times 1024 \times 256$	8.19	381.45
7	5×10^{-6}	3.3×10^{8}	28.21	0.09	2	$1024 \times 1024 \times 256$	9.06	442.90
8	5×10^{-6}	4×10^{8}	34.20	0.10	2	$1024 \times 1024 \times 256$	12.39	582.74
9	5×10^{-6}	5×10^{8}	42.75	0.11	2	$1152 \times 1152 \times 288$	17.07	761.06
10	5×10^{-6}	7×10^{8}	59.85	0.13	2	$1536 \times 1536 \times 384$	26.23	1084.40
11	5×10^{-6}	1×10^{9}	85.50	0.16	1	$864 \times 864 \times 432$	39.82	1525.94
12	5×10^{-6}	2×10^{9}	171.00	0.22	1	$864 \times 864 \times 432$	70.69	2649.10
13	5×10^{-6}	3×10^{9}	256.50	0.27	1	$864 \times 864 \times 432$	94.81	3463.90
14	5×10^{-6}	5×10^{9}	427.49	0.35	1	$864 \times 864 \times 432$	125.94	4644.18

Table 2. For caption see next page.

Case no.	Ek	Ra	$\widetilde{Ra}$	Ro	Γ	$N_x \times N_y \times N_z$	Nu	Re
15	5×10^{-6}	7×10^{9}	598.49	0.42	1	1024 × 1024 × 512	148.57	5398.48
16	5×10^{-6}	1×10^{10}	854.99	0.50	1	1024 × 1024 × 512	178.13	6588.07
17	5×10^{-6}	3×10^{10}	2564.96	0.87	1	1280 × 1280 × 640	297.46	12 560.09
18	5×10^{-6}	5×10^{10}	4274.94	1.12	1	1536 × 1536 × 960	365.17	16 443.62
19	5×10^{-6}	7×10^{10}	5984.92	1.32	0.5	864 × 864 × 1024	402.27	18 708.38
20	5×10^{-6}	1×10^{11}	8549.88	1.58	0.5	864 × 864 × 1024	463.27	22 532.78
21	5×10^{-7}	4×10^{9}	5.87	0.03	1	864 × 864 × 432	2.76	281.02
22	5×10^{-7}	4.3×10^{9}	17.06	0.03	1	864 × 864 × 432	3.14	324.89
23	5×10^{-7}	5×10^{9}	19.84	0.04	1	864 × 864 × 432	4.16	438.65
24	5×10^{-7}	6.3×10^{9}	25.00	0.04	1	864 × 864 × 432	6.63	703.30
25	5×10^{-7}	8.3×10^{9}	32.94	0.05	1	864 × 864 × 432	10.30	1124.74
26	5×10^{-7}	1×10^{10}	39.69	0.05	1	1024 × 1024 × 512	13.57	1433.84
27	5×10^{-7}	1.3×10^{10}	51.59	0.06	1	1152 × 1152 × 576	20.13	1978.18
28	5×10^{-7}	2×10^{10}	79.37	0.07	1	1920 × 1920 × 960	39.90	3479.12
29	5×10^{-7}	3×10^{10}	119.06	0.09	0.25	512 × 512 × 512	81.92	5898.88
30	5×10^{-7}	5×10^{10}	198.43	0.11	1	1920 × 1920 × 960	139.11	7621.40
31	5×10^{-7}	7×10^{10}	277.80	0.13	0.25	512 × 512 × 512	175.77	10 983.34
32	5×10^{-7}	1×10^{11}	396.85	0.16	0.25	864 × 864 × 864	217.55	14 073.71
33	5×10^{-7}	1.5×10^{11}	595.28	0.19	0.25	960 × 960 × 960	283.78	15 982.90
34	5×10^{-7}	3×10^{11}	1190.55	0.27	0.25	960 × 960 × 960	462.30	25 800.00
35	5×10^{-8}	7×10^{10}	12.89	0.01	0.5	1152 × 1152 × 576	1.57	154.64
36	5×10^{-8}	8×10^{10}	14.74	0.01	0.25	480 × 480 × 640	2.00	503.79
37	5×10^{-8}	9×10^{10}	16.58	0.02	0.25	480 × 480 × 640	2.47	770.47
38	5×10^{-8}	1×10^{11}	18.42	0.02	0.25	480 × 480 × 640	3.57	805.27
39	5×10^{-8}	1.1×10^{11}	20.26	0.02	0.25	576 × 576 × 768	4.17	965.57
40	5×10^{-8}	1.2×10^{11}	22.10	0.02	0.25	576 × 576 × 768	4.88	1119.23
41	5×10^{-8}	1.3×10^{11}	23.95	0.02	0.25	576 × 576 × 768	5.61	1296.02
42	5×10^{-8}	1.5×10^{11}	27.63	0.02	0.25	576 × 576 × 768	7.25	1704.47
43	5×10^{-8}	1.7×10^{11}	31.31	0.02	0.25	576 × 576 × 768	8.72	2110.53
44	5×10^{-8}	2×10^{11}	36.84	0.02	0.25	768 × 768 × 768	11.01	2632.32
45	5×10^{-8}	3×10^{11}	55.26	0.03	0.25	768 × 768 × 768	19.39	4325.23
46	5×10^{-8}	4×10^{11}	73.68	0.03	0.25	768 × 768 × 768	30.02	6129.86
47	5×10^{-8}	5×10^{11}	92.10	0.04	0.125	480 × 480 × 960	46.92	8761.22
48	5×10^{-8}	7×10^{11}	128.94	0.04	0.125	480 × 480 × 960	89.61	13 450.07
49	5×10^{-8}	1×10^{12}	184.20	0.05	0.125	512 × 512 × 1024	164.24	23 131.98
50	5×10^{-8}	2×10^{12}	368.40	0.07	0.125	512 × 512 × 1024	349.22	37 891.22
51	5×10^{-8}	3×10^{12}	552.60	0.09	0.25	1920 × 1920 × 1920	574.52	53 135.11
52	5×10^{-8}	5×10^{12}	921.01	0.11	0.125	768 × 768 × 1536	936.30	77 889.37

Table 2. (cntd). Summary of the parameters considered in this study: Ek is the Ekman number, Ra is the Rayleigh number, $\widetilde{Ra} \equiv Ra\, Ek^{4/3}$ is the reduced Rayleigh number, $Ro = \sqrt{Ra/Pr}\, Ek$ is the convective Rossby number, Γ is the ratio of the width to the height of the computational domain, Nu is the Nusselt number, and Re is the Reynolds number, computed from the root mean square of the vertical component of velocity. The Prandtl number Pr is fixed at 1 for all simulations.

REFERENCES

AGUIRRE GUZMÁN, A.J., MADONIA, M., CHENG, J.S., OSTILLA-MÓNICO, R., CLERCX, H.J.H. & KUNNEN, R.P.J. 2021 Force balance in rapidly rotating Rayleigh–Bénard convection. *J. Fluid Mech.* **928**, A16.

AHLERS, G., GROSSMANN, S. & LOHSE, D. 2009 Heat transfer and large scale dynamics in turbulent Rayleigh–Bénard convection. *Rev. Mod. Phys.* **81** (2), 503–537.

ATKINSON, B.W. & ZHANG, J.W. 1996 Mesoscale shallow convection in the atmosphere. *Rev. Geophys.* **34** (4), 403–431.

AURNOU, J.M., CALKINS, M.A., CHENG, J.S., JULIEN, K., KING, E.M., NIEVES, D., SODERLUND, K.M. & STELLMACH, S. 2015 Rotating convective turbulence in Earth and planetary cores. *Phys. Earth Planet. Inter.* **246**, 52–71.

AURNOU, J.M., HORN, S. & JULIEN, K. 2020 Connections between nonrotating, slowly rotating, and rapidly rotating turbulent convection transport scalings. *Phys. Rev. Res.* **2** (4), 043115.

BOUILLAUTA, V., MIQUELA, B., JULIEN, K., AUMAÎTRE, S. & GALLET, B. 2021 Experimental observation of the geostrophic turbulence regime of rapidly rotating convection. *Proc. Natl Acad. Sci. USA* **118** (44), e2105015118.

CALZAVARINI, E., LOHSE, D., TOSCHI, F. & TRIPICCIONE, R. 2005 Rayleigh and Prandtl number scaling in the bulk of Rayleigh–Bénard turbulence. *Phys. Fluids* **17** (5), 055107.

CHANDRASEKHAR, S. 1961 *Hydrodynamic and Hydromagnetic Stability*. Oxford University Press.

CHENG, J.S. & AURNOU, J.M. 2016 Tests of diffusion-free scaling behaviors in numerical dynamo datasets. *Earth Planet. Sci. Lett.* **436**, 121–129.

CHENG, J.S., STELLMACH, S., RIBEIRO, A., GRANNAN, A., KING, E.M. & AURNOU, J.M. 2015 Laboratory-numerical models of rapidly rotating convection in planetary cores. *Geophys. J. Intl* **201** (1), 1–17.

CHRISTENSEN, U.R. & AUBERT, J. 2006 Scaling properties of convection-driven dynamos in rotating spherical shells and application to planetary magnetic fields. *Geophys. J. Intl* **166** (1), 97–114.

DE WIT, X.M., VAN KAN, A. & ALEXAKIS, A. 2022 Bistability of the large-scale dynamics in quasi-two-dimensional turbulence. *J. Fluid Mech.* **939**, R2.

ECKE, R.E. & SHISHKINA, O. 2023 Turbulent rotating Rayleigh–Bénard convection. *Annu. Rev. Fluid Mech.* **55** (1), 603–638.

FAVIER, B., GUERVILLY, C. & KNOBLOCH, E. 2019 Subcritical turbulent condensate in rapidly rotating Rayleigh–Bénard convection. *J. Fluid Mech.* **864**, R1.

FAVIER, B., SILVERS, L.J. & PROCTOR, M.R.E. 2014 Inverse cascade and symmetry breaking in rapidly rotating Boussinesq convection. *Phys. Fluids* **26** (9), 096605.

GILLET, N. & JONES, C.A. 2006 The quasi-geostrophic model for rapidly rotating spherical convection outside the tangent cylinder. *J. Fluid Mech.* **554**, 343–369.

GREENSPAN, H.P. 1969 *The Theory of Rotating Fluids*. Cambridge University Press.

GROSSMANN, S. & LOHSE, D. 2004 Fluctuations in turbulent Rayleigh–Bénard convection: the role of plumes. *Phys. Fluids* **16** (12), 4462–4472.

GUBBINS, D. 2001 The Rayleigh number for convection in the Earth's core. *Phys. Earth Planet Inter.* **128** (1–4), 3–12.

GUERVILLY, C., CARDIN, P. & SCHAEFFER, N. 2019 Turbulent convective length scale in planetary cores. *Nature* **570** (7761), 368–371.

GUERVILLY, C., HUGHES, D.W. & JONES, C.A. 2014 Large-scale vortices in rapidly rotating Rayleigh–Bénard convection. *J. Fluid Mech.* **758**, 407–435.

INCROPERA, F.P. & DEWITT, D.P. 1996 *Fundamentals of Heat and Mass Transfer*. 4th edn. John Wiley & Sons, Inc.

JULIEN, K., AURNOU, J.M., CALKINS, M.A., KNOBLOCH, E., MARTI, P., STELLMACH, S. & VASIL, G.M. 2016 A nonlinear model for rotationally constrained convection with Ekman pumping. *J. Fluid Mech.* **798**, 50–87.

JULIEN, K., KNOBLOCH, E., RUBIO, A.M. & VASIL, G.M. 2012*a* Heat transport in low-Rossby-number Rayleigh–Bénard convection. *Phys. Rev. Lett.* **109** (25), 254503.

JULIEN, K., RUBIO, A.M., GROOMS, I. & KNOBLOCH, E. 2012*b* Statistical and physical balances in low Rossby number Rayleigh–Bénard convection. *Geophys. Astrophys. Fluid Dyn.* **106** (4–5), 392–428.

VAN KAN, A., JULIEN, K., MIQUEL, B. & KNOBLOCH, E. 2024 Bridging the Rossby number gap in rapidly rotating thermal convection. arXiv preprint arXiv: 2409.08536.

KING, E.M., STELLMACH, S. & AURNOU, J.M. 2012 Heat transfer by rapidly rotating Rayleigh–Bénard convection. *J. Fluid Mech.* **691**, 568–582.

KING, E.M., STELLMACH, S., NOIR, J., HANSEN, U. & AURNOU, J.M. 2009 Boundary layer control of rotating convection systems. *Nature* **457** (7227), 301–304.

KRAICHNAN, R.H. 1962 Turbulent thermal convection at arbitrary Prandtl number. *Phys. Fluids* **5** (11), 1374–1389.

KUNNEN, R.P.J. 2021 The geostrophic regime of rapidly rotating turbulent convection. *J. Turbul.* **22** (4–5), 267–296.

KUNNEN, R.P.J., OSTILLA-MÓNICO, R., VAN DER POEL, E.P., VERZICCO, R. & LOHSE, D. 2016 Transition to geostrophic convection: the role of the boundary conditions. *J. Fluid Mech.* **799**, 413–432.

LOHSE, D. & SHISHKINA, O. 2024 Ultimate Rayleigh–Bénard turbulence. *Rev. Mod. Phys.* **96** (3), 035001.

LOHSE, D. & TOSCHI, F. 2003 Ultimate state of thermal convection. *Phys. Rev. Lett.* **90** (3), 034502.

MAFFEI, S., KROUSS, M.J., JULIEN, K. & CALKINS, M.A. 2021 On the inverse cascade and flow speed scaling behaviour in rapidly rotating Rayleigh–Bénard convection. *J. Fluid Mech.* **913**, A18.

MALKUS, W.V.R. 1954 The heat transport and spectrum of thermal turbulence. *Proc. R. Soc. Lond. A* **225** (1161), 196–212.

MARSHALL, J. & SCHOTT, F. 1999 Open-ocean convection: observations, theory, and models. *Rev. Geophys.* **37** (1), 1–64.

OLIVER, T.G., JACOBI, A.S., JULIEN, K. & CALKINS, M.A. 2023 Small scale quasigeostrophic convective turbulence at large Rayleigh number. *Phys. Rev. Fluids* **8** (9), 093502.

PETSCHEL, K., STELLMACH, S., WILCZEK, M., LÜLFF, J. & HANSEN, U. 2013 Dissipation layers in Rayleigh–Bénard convection: a unifying view. *Phys. Rev. Lett.* **110** (11), 114502.

PLUMLEY, M. & JULIEN, K. 2019 Scaling laws in Rayleigh–Bénard convection. *Earth Space Sci.* **6** (9), 1580–1592.

PLUMLEY, M., JULIEN, K., MARTI, P. & STELLMACH, S. 2017 Sensitivity of rapidly rotating Rayleigh–Bénard convection to Ekman pumping. *Phys. Rev. Fluids* **2** (9), 094801.

VAN DER POEL, E.P., OSTILLA-MÓNICO, R., DONNERS, J. & VERZICCO, R. 2015 A pencil distributed finite difference code for strongly turbulent wall–bounded flows. *Comput. Fluids* **116**, 10–16.

RUBIO, A.M., JULIEN, K., KNOBLOCH, E. & WEISS, J.B. 2014 Upscale energy transfer in three-dimensional rapidly rotating turbulent convection. *Phys. Rev. Lett.* **112** (14), 144501.

SCHEEL, J.D., EMRAN, M.S. & SCHUMACHER, J. 2013 Resolving the fine-scale structure in turbulent Rayleigh–Bénard convection. *New J. Phys.* **15** (11), 113063.

SHISHKINA, O., STEVENS, R.J.A.M., GROSSMANN, S. & LOHSE, D. 2010 Boundary layer structure in turbulent thermal convection and its consequences for the required numerical resolution. *New J. Phys.* **12** (7), 075022.

SONG, J., KANNAN, V., SHISHKINA, O. & ZHU, X. 2024*a* Direct numerical simulations of the transition between rotation- to buoyancy-dominated regimes in rotating Rayleigh–Bénard convection. *Intl J. Heat Mass Transfer* **232**, 125971.

SONG, J., SHISHKINA, O. & ZHU, X. 2024*b* Direct numerical simulations of rapidly rotating Rayleigh–Bénard convection with Rayleigh number up to 5×10^{13}. *J. Fluid Mech.* **989**, A3.

SONG, J., SHISHKINA, O. & ZHU, X. 2024*c* Scaling regimes in rapidly rotating thermal convection at extreme Rayleigh numbers. *J. Fluid Mech.* **984**, A45.

SPRAGUE, M., JULIEN, K., KNOBLOCH, E. & WERNE, J. 2006 Numerical simulation of an asymptotically reduced system for rotationally constrained convection. *J. Fluid Mech.* **551**, 141–174.

SREENIVASAN, B. & JONES, C.A. 2006 The role of inertia in the evolution of spherical dynamos. *Geophys. J. Intl* **164** (2), 467–476.

STELLMACH, S., LISCHPER, M., JULIEN, K., VASIL, G., CHENG, J.S., RIBEIRO, A., KING, E.M. & AURNOU, J.M. 2014 Approaching the asymptotic regime of rapidly rotating convection: boundary layers versus interior dynamics. *Phys. Rev. Lett.* **113** (25), 254501.

STEVENS, R.J.A.M., CLERCX, H.J.H. & LOHSE, D. 2013 Heat transport and flow structure in rotating Rayleigh–Bénard convection. *Eur. J. Mech.* **40**, 41–49.

STEVENS, R.J.A.M., VERZICCO, R. & LOHSE, D. 2010 Radial boundary layer structure and Nusselt number in Rayleigh–Bénard convection. *J. Fluid Mech.* **643**, 495–507.

STEVENSON, D.J. 1979 Turbulent thermal convection in the presence of rotation and a magnetic field – a heuristic theory. *Geophys. Astrophys. Fluid Dyn.* **12** (1), 139–169.

TOSELLI, F., MUSACCHIO, S. & BOFFETTA, G. 2019 Effects of rotation on the bulk turbulent convection. *J. Fluid Mech.* **881**, 648–659.

VERZICCO, R. & CAMUSSI, R. 2003 Numerical experiments on strongly turbulent thermal convection in a slender cylindrical cell. *J. Fluid Mech.* **477**, 19–49.

VERZICCO, R. & ORLANDI, P. 1996 A finite-difference scheme for three-dimensional incompressible flow in cylindrical coordinates. *J. Comput. Phys.* **123** (2), 402–413.

WICHT, J. & SANCHEZ, S. 2019 Advances in geodynamo modelling. *Geophys. Astrophys. Fluid Dyn.* **113** (1–2), 2–50.

ZHONG, J. & AHLERS, G. 2010 Heat transport and the large-scale circulation in rotating turbulent Rayleigh–Bénard convection. *J. Fluid Mech.* **665**, 300–333.

ZHU, X. *et al.* 2018 AFiD-GPU: a versatile Navier–Stokes solver for wall-bounded turbulent flows on GPU clusters. *Comput. Phys. Commun.* **229**, 199–210.